# Helium implantation in Si (100): swelling, microstructure, and mechanical property changes

Xi Huang<sup>1</sup>, Yujun Xie<sup>1,2,\*</sup>, Mehdi Balooch<sup>1</sup>, Sean Lubner<sup>3,4</sup>, and Peter Hosemann<sup>1,5,\*</sup>

<sup>1</sup> Department of Nuclear Engineering, University of California Berkeley, Berkeley, CA 94704, USA

<sup>2</sup> National Center for Electron Microscopy, Molecular Foundry, Lawrence Berkeley National

Laboratory, Berkeley, CA 94720, USA

<sup>3</sup> Energy Storage & Distributed Resources Division, Lawrence Berkeley National Laboratory,

Berkeley CA 94720, USA

<sup>4</sup> Research Laboratory of Electronics, Massachusetts Institute of Technology, Cambridge, MA 02139, USA

<sup>5</sup> Materials Sciences Division, Lawrence Berkeley National Laboratory, Berkeley CA 94720, USA

\*Corresponding authors: terryxie007@lbl.gov (Yujun Xie)

peterh@berkeley.edu (Peter Hosemann)

### **Abstract**

Microstructural changes induced by Helium implantation in materials lead to volumetric swelling and mechanical property changes. How these properties are linked and establishing direct relationships can be difficult due to the underlying materials microstructure evolution. Some materials also experience a phase change due to irradiation damage making it even more complex to analyze. Here, single crystalline Si (100) was used to establish a relationship among these parameters. The swelling height as a function of implantation fluence can equally fit a linear relationship. Solely irradiation induced defects are observed at low fluence below  $5.0 \times 10^{16}$  ions/cm<sup>2</sup>. An abrupt amorphous and crystalline mixed layer of ~200 nm thick within highly damaged polycrystalline matrix is observed when implantation fluence exceeds  $5.0 \times 10^{16}$  ions/cm<sup>2</sup>, leading to the appearance of irradiation induced swelling and hardening behavior. As the fluence increases beyond  $1.0 \times 10^{17}$  ions/cm<sup>2</sup>, the amorphous layer expands in size and the bubble size distribution takes the form of a Gaussian distribution with a maximum size of up to 6.4 nm, which causes a further increase in the height of swelling. Furthermore, irradiation induced softening appeared due to the enlarged bubble size and amorphization.

**Keywords:** Si, Helium implantation, Swelling behavior, Micromechanical properties, Hardness and reduced modulus

#### 1. Introduction

Ion irradiation techniques are widely employed to evaluate the irradiation damage and swelling behavior of materials in nuclear applications since they can generate high damage rates without significant residual radioactivity and at lower cost compared to neutron irradiation <sup>1,2</sup>. The technique has also been adopted as a tool to introduce controllable concentrations of defects at precise depths in the semiconductors field <sup>3</sup>. The introduction of defects will lead to changes in microstructure of semiconductor and insulator materials, resulting in a wide variation in physical behaviors, including electrical and optical properties <sup>4</sup>. Small irradiating beam spot sizes also allow heterogeneous alterations of mechanical properties with <10 nm resolution. This could enable new approaches to creating cryogenic phononic metamaterials by patterning sub-wavelength features <sup>5–7</sup>, such as to shield qubits from deleterious phonons in quantum computers or increase the detection efficiency of dark matter detectors by better guiding collision-generated phonons to detectors. Therefore, major efforts have been made to understand the effect of ion irradiation in the semiconductor materials field in the past few decades, especially on Si, the most important material in the semiconductor industry today <sup>3,8,9</sup>.

The formation of Helium bubbles in Si due to ion beam implantation was first reported by C.C. Griffioen et al. <sup>10</sup>. Since then the underlying mechanisms and their possible applications in the semiconductor industry have extensively been investigated <sup>11</sup>. Summarizing the previous research results, it is found that the formation of He bubbles in Si is affected by multiple factors: implantation dose, dose rate, energy<sup>12,13</sup>, temperature <sup>14,15</sup>, and post implantation thermal treatments <sup>16,17</sup> among others. The formation of bubbles is accompanied by the change of the density of Si, which will result in swelling <sup>18–21</sup>. S. Momota et al. investigated the swelling behavior of Si under Ar<sup>+</sup> implantation and concluded that swelling height increases with the increasing of implantation fluence and energy <sup>20</sup>. J. Zhang et al. studied the annealing temperature on the swelling behavior of Ar<sup>+</sup> implanted Si and reported that swelling height varies with annealing temperature <sup>21</sup>. M. Ikeyama et al. found that He implantation induced swelling becomes saturated over 1.0×10<sup>15</sup> ions/cm<sup>2</sup> regardless of implantation energy, and the maximum swelling height is almost proportional to implantation fluence <sup>18</sup>. So far, the swelling

behavior of Si under He implantation has been, however, examined at the lower limits of implantation fluences: such as  $8.0 \times 10^{16} \, ^{21}$ ,  $8.0 \times 10^{16} \, ^{20}$ ,  $6.0 \times 10^{16} \, ^{19}$  and  $1 \sim 2.0 \times 10^{17} \, ions/cm^2 \, ^{18}$ . The swelling behavior of Si is still unknown when implantation fluence reaches a higher level of about  $1.0 \times 10^{18} \, ions/cm^2$  or beyond. Of particular interest is finding a correlation between volumetric swelling and changes in micromechanical and thermal properties of single crystal Si under He implantation. Conducting the study on a single crystal allows to study the effects without the influence of underlying microstructure such as grain boundaries that further complicates the studies.

The current work presents a relationship among the swelling height, microstructure, and corresponding micromechanical properties of a single crystal Si under He implantation beyond the range of fluences reported before. The Si (100) was implanted by 25 keV He with the fluences of  $5.0\times10^{16}$ ,  $1.0\times10^{17}$ ,  $2.0\times10^{17}$ ,  $5.0\times10^{17}$ ,  $7.5\times10^{17}$ , and  $1.0\times10^{18}$  ions/cm<sup>2</sup>. Following implants, the swelling behavior, microstructure, and micromechanical properties of implanted Si were evaluated by advanced techniques of AFM, SEM, and TEM.

# 2. Experimental procedures

A high-purity (>99.99%) undoped single-crystal Si (100) sample was used as the target in this investigation. The Helium implantation experiments were conducted at room temperature (RT) using the focused helium ion beam of a Zeiss ORION NanoFab HIM operated at 25 keV. The ion beam had a few nanometers that scanned over the sample with a diameter incident perpendicular to the surface. The sputtering yield of a 25 keV beam on Si was less than 5×10<sup>-222</sup>. The implants performed at different fluences covering an order of magnitude, each covering 10 × 10 μm<sup>2</sup> area on the same sample. The beam current was maintained at ~100 pA during implants while reduced to ~1 pA for imaging to avoid significant additional implants. The profile of displacement damage in units of displacement per atom (dpa) and ions distribution were calculated using the Stopping and Range of Ions in Matter (SRIM-2013) code based on the full damage cascades (F-C) model <sup>23</sup>. The threshold displacement energy, lattice binding energy, and surface binding energy used in this investigation were 40, 3.25, and 4.7 eV, respectively<sup>24</sup>. The SRIM use in the present studies, however, does not account for

porosity, crystal orientation or structure. The displacement damage profile and ion distribution in Si (100) implanted with a total fluence of  $5.0 \times 10^{16}$ ,  $1.0 \times 10^{17}$ ,  $2.0 \times 10^{17}$ ,  $7.5 \times 10^{17}$  and  $1.0 \times 10^{18}$  ions/cm<sup>2</sup> are shown in Fig. 1. The peak values of He concentration are  $\underline{5.5 \times 10^4}$ ,  $\underline{1.1 \times 10^5}$ ,  $\underline{2.2 \times 10^5}$ ,  $\underline{8.3 \times 10^5}$ , and  $1.1 \times 10^6$  atomic parts per million (appm) at a depth of ~275 nm for doses of approximately  $\underline{1.4}$ ,  $\underline{2.8}$ ,  $\underline{5.5}$ ,  $\underline{20.7}$ , and  $\underline{27.6}$  dpa, respectively.

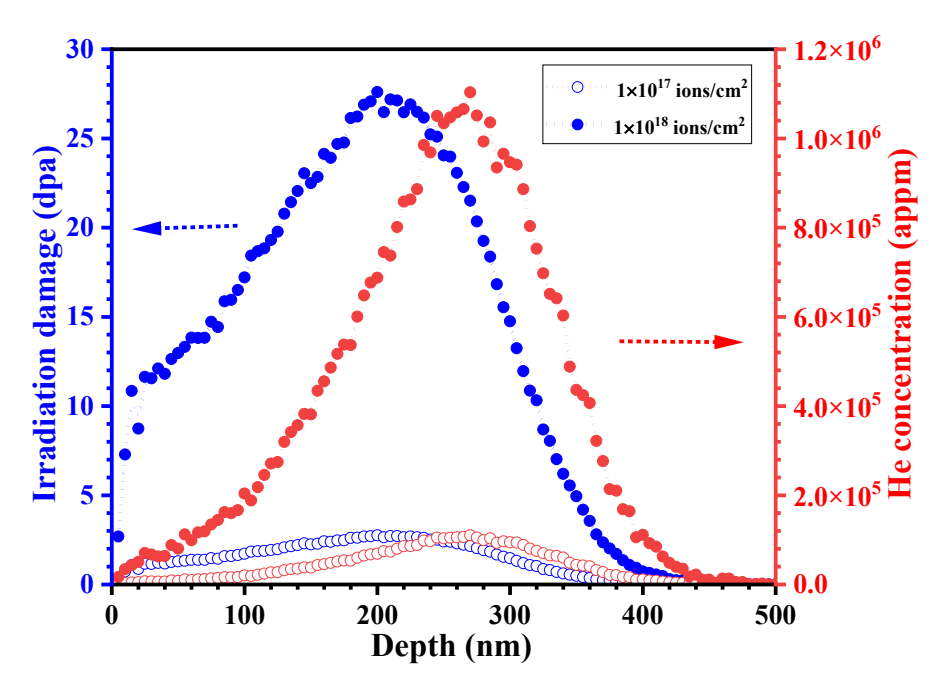


Figure 1 The displacement damage profile and ions distribution in Si (001) subjected to He ion implantation at 25 keV with different fluences.

An atomic force microscopy (AFM), Nanoscope III made by Digital Instruments Inc., was used to analyze the changes of surface topography, roughness and swelling. Following the AFM imaging, the irradiated sample was attached firmly on iron puck using crystal bond, and subsequently mounted on the magnetic stage of TI950. The mechanical properties of the samples within and off implanted areas were tested using a Hysitron TI 950 TriboIndenter using a diamond Berkovich indenter tip with a nominal radius of curvature of 50 nm that was calibrated in advance against fused silica. Continuous Stiffness Measurement (CSM) mode was employed to test the hardness and elastic modulus of implanted samples at different depths. The maximum penetration depth is controlled between 200 and 250 nm in the present

investigation. For each area, nine indentations were taken to obtain the average hardness and elastic modulus and their standard deviations.

Thin-foil samples for transmission electron microscope (TEM) were prepared using a Helios NanoLab 600i dual-beam focused ion beam (DB-FIB) with a Ga ion sputtering after a protective Pt layer was deposited on the implanted area. Microstructure and selected area electron diffraction (SAED) analysis were conducted on 300 kV JEOL 3010 at the national center for electron microscopy of Lawrence Berkeley National Laboratory.

#### 3. Results and discussions

Fig. 2 shows the AFM surface topographic images and corresponding swelling height of implanted areas with different fluences ranging from 1.0×10<sup>17</sup> to 1.0×10<sup>18</sup> ions/cm<sup>2</sup>. The swelling height of samples implanted with 5.0×10<sup>16</sup> ions/cm<sup>2</sup> is not illustrated in Fig. 2 because the swelling height was below the uncertainty level of AFM measurements in our laboratory. The outline of the implanted area gradually becomes clear with the increasing of fluences, indicating that swelling height gradually increases with the rise of implantation fluences. The swelling height of the edge region measures higher than that of the middle region: for example, the former is 47 nm for  $5.0 \times 10^{17}$  ions/cm<sup>2</sup> and the letter is 42 nm. Furthermore, the difference between these two regions gradually increases with increasing fluences, except for 1.0×10<sup>18</sup> ions/cm<sup>2</sup> that no measurable differences is observed. Since He bubbles are not formed at low implantation fluences, the phenomenon may due to the stress concentration caused by volume change during the amorphization process. The amorphous transformation leads to the severe distortion of the lattice <sup>25</sup>, resulting in the swelling. The swelling will bring a high stress concentration in the irradiated regions <sup>26</sup>. In order to relax the stress, the stress gradually concentrates at the edge region and then leads to a high swelling height. The sample implanted with high fluences ,results in formation of high pressure bubbles that facilitates expansion in the direction normal to the surface more effectively.<sup>27</sup> Therefore, the excessive edge height effect diminishes.

Average values of 5.6, 15.5, 42.0 and 97.0 nm are evaluated for the fluences of  $1.0 \times 10^{17}$ ,  $2.0 \times 10^{17}$ ,  $5.0 \times 10^{17}$  and  $1.0 \times 10^{18}$  ions/cm<sup>2</sup>, respectively. It appears that the swelling height as a function of dose follows a linear relationship, as shown in Fig. 2. This result is different from that of reported by P.K. Giri et al., who investigated the swelling mechanism of Si under low energy self-ion irradiation (80 keV) and found that the swelling height follows a linear relationship with a cube root dependence on the fluences <sup>19</sup>. It is well stablished that the swelling height of Si is caused by the synergy effect of defects, He bubbles and amorphization <sup>19,28</sup>. S.Eichler et al. investigated the defects in Si after B<sup>+</sup> implantation and reported that the defect concentration increases proportionally to the square root of the fluences <sup>29</sup>. What's more, Sealy et al. further confirmed this result by measuring the integrated strain of Si by X-ray diffraction <sup>30</sup>. Besides, P.K. Giri et al.'s results revealed that the cube root relationship is caused by the effect of concentration of vacancy type defects in Si and found no irradiation induced amorphization and He bubbles formation in their studies <sup>19</sup>. However, the fluence of the selfions there was rather low (6.0×10<sup>16</sup> ions/cm<sup>2</sup>) and therefore only the generation of vacancies are considered. In the present work, we experience the effect of Helium bubble formation, amorphization and the generation of vacancies individually, depending on range of ion fluence is applied. Previous investigations have confirmed that the existence of helium bubbles and amorphous layer will lead to the swelling of Si 31. For example, K.J. Abrams et al. studied the helium irradiation effects in polycrystalline Si, and directly observed the increase in the width of Si layer due to the microstructure change of He bubbles <sup>31</sup>. Meanwhile, the swelling behavior of SiC under helium implantation was studied by S. Leclerc et al., and they reported that the contribution of amorphous to the swelling height is about 15% of the amorphous layer thickness <sup>28</sup>. It is known that the density of amorphous Si is 1.8% lower than that of crystalline Si <sup>32</sup>, which would lead to ~7 nm height increase assuming the entire penetration depth amorphized. This seems to be close to magnitude for 1.0×10<sup>17</sup> ions/cm<sup>2</sup> implantation. It is worth mentioning in the present study that no blistering is observed even if the implantation fluence reaches 1.0×10<sup>18</sup> ions/cm<sup>2</sup>. It may be possible that the threshold at which blistering occurs is beyond the maximum does we used here, unlike metals such as W reported recently by F.I. Allen et al., due to the limited ductility of the material <sup>33</sup>.

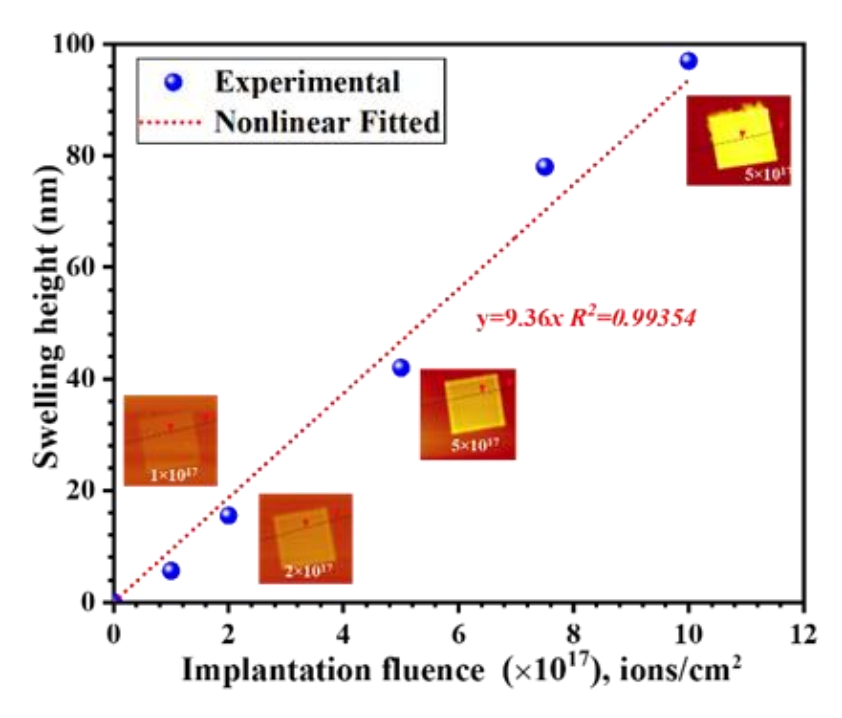


Figure 2 AFM surface topographic images and corresponding swelling height of implanted areas with different fluences ranging from 1.0×10<sup>17</sup> to 1.0×10<sup>18</sup> ions/cm<sup>2</sup>.

Fig. 3 displays the cross-sectional TEM images and corresponding selected area electron diffraction (SAED) patterns of Si implanted with He ions to a fluence of 5.0×10<sup>16</sup> ions/cm<sup>2</sup>. No detectable He bubbles are observed, while irradiation induced defects are visible in bright-filed TEM, as shown in Fig. 3 (a). The absence of helium bubbles indicates that irradiation induced bubbles in Si are in the stage of nucleation or perhaps incubation rather than growth. Besides, SAED patterns in the implanted area, as shown in Fig. 3 (b), also reveals that no irradiation induced amorphization occurs as the irradiation fluence increases up to 5.0×10<sup>16</sup> ions/cm<sup>2</sup>. Weak diffuse rings are observed on both implanted and unimplanted region, as shown in Fig. 3 (b) and (c), that maybe the results of TEM slice using FIB rather than ion irradiation preparation. Previous investigations on the crystalline to amorphous transition in Si under He implantation also reported a similar result, though different experiments show slight different threshold fluence to occur.<sup>34–36</sup> For instance, no irradiation induced amorphization was observed in Si implanted with He at energies between 20 and 300 keV with the fluence less

than  $1.0 \times 10^{17}$  ions/cm<sup>2</sup> <sup>34</sup>. But, an amorphized layer was formed when a fluence of  $2.5 \times 10^{17}$  He atoms/cm<sup>2</sup> at 20 keV was implanted into Si at RT<sup>35</sup>. Summarizing the results of these experiments, it can be found that the amorphization of Si occurs for a fluence near  $1.0 \times 10^{17}$  cm<sup>-2</sup>. Besides, it also should be pointed out that most of investigations on the amorphization of Si only state a fluence and rough numbers to quantify this behavior rather than dpa <sup>34–36</sup>. In current experiments, the maximum dpa at a fluence of  $5.0 \times 10^{16}$  ions/cm<sup>2</sup> is about <u>1.4</u> dpa, as shown in Fig. 1, and therefore we can infer that the threshold of amorphization in Si should be larger than the above-mentioned value.

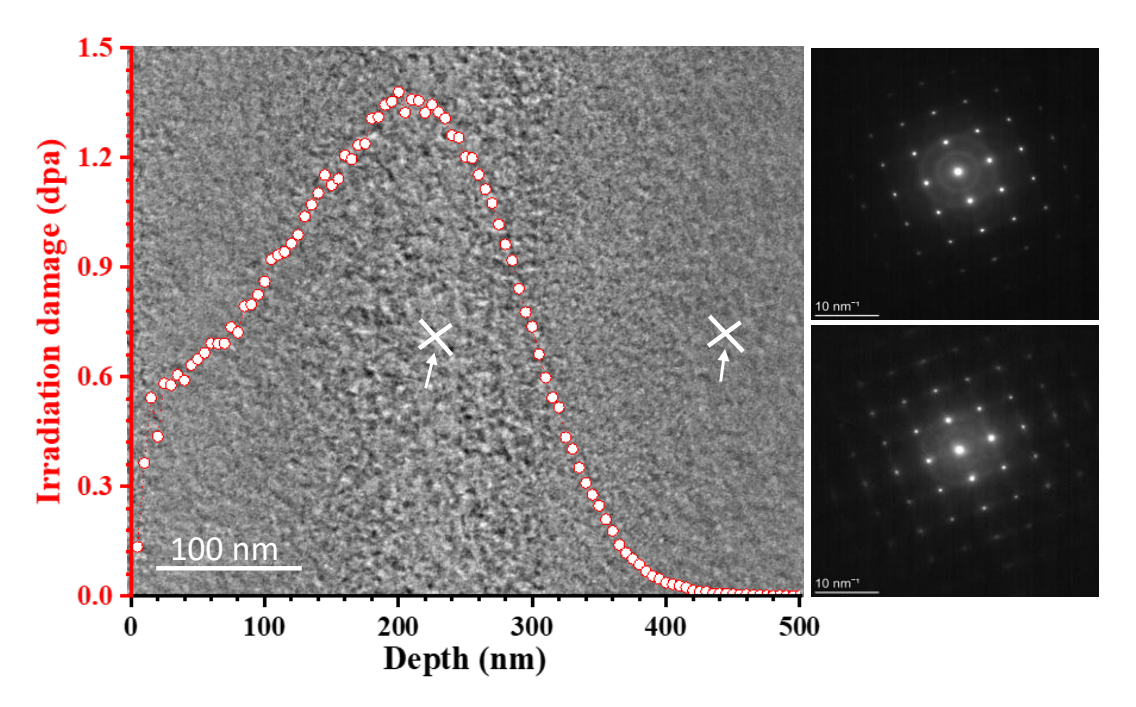


Figure 3 The cross-sectional TEM image and corresponding SAED patterns of Si implanted with He to a fluence of 5.0×10<sup>16</sup> ions/cm<sup>2</sup>: (a) the cross-sectional TEM image of implanted layer; (b) and (c) the SAED patterns at different positions marked in image (a).

Fig. 4 displays the cross-sectional TEM images and corresponding Fast Fourier Transform (FFT) patterns of Si implanted with He ions to a fluence of  $1.0 \times 10^{17}$  ions/cm<sup>2</sup>. An obvious band of about 200 nm appears at the peak of irradiation damage, as shown in Fig. 4 (c). A larger number of bubbles are observed in this 'band' when TEM the sample is overfocused, as shown in Fig. 4 (d). The average size of the bubbles is around  $1\sim2$  nm when the TEM image is further enlarged, as shown in Fig. 4 (f), and they are uniformly distributed within the 'band'. The formation of a void layer free of any interstitial-type defects in Si was also reported by M.L.

David et al., who investigated the stability of defects created by high fluence helium implantation (50 keV, 5.0×10<sup>16</sup> ions/cm<sup>2</sup>) from RT to 800 °C <sup>37</sup>. However, K.E. Haynes found the formation of a mixed layer of defects and helium bubbles in Si implanted with helium of a fluence of 4.0×10<sup>16</sup> ions/cm<sup>2</sup> at 0.5 keV and RT <sup>38</sup>. The difference may be attributed to the implantation energy and rate differences between their work and present investigation. The higher the implantation energy and the rate, the larger He bubble and lower density formation is expected <sup>38</sup>. An increase in the size of bubbles will absorb more vacancies and interstitial clusters, resulting in a low number of defects around He bubbles.

The 'band' contains mixed amorphous and undisturbed matrix layers as evident from FFT analysis of high-resolution electron microscopy, as shown in Fig. 4 (b). This result suggests that the helium implantation partially induces the amorphization of single crystal Si around a fluence of 1.0×10<sup>17</sup> ions/cm<sup>2</sup>. This is in good agreement with the results of Reutov and Sokhatskii <sup>36</sup>, who also suggested a threshold of 10<sup>17</sup> ions/cm<sup>2</sup> at RT. In addition, F.F. Morehead and B.L. Crowder proposed that the critical temperature to occur the transition from crystalline to amorphous in Si by B<sup>+</sup> implantation is 33 °C <sup>39</sup>. Therefore, it can be inferred that the critical temperature for current experiments should be higher than B<sup>+</sup> implantation because He is lighter than B <sup>35</sup>. However, in current work, amorphization takes place in Si implanted at RT, which is lower than expectation. It has been established that amorphous region is formed in the atomic collision cascades according to the principal accumulation of irradiation induced defects will favor the amorphization of Si 40. In current work, the low temperature of implantation ensures a low rate of the pair recombination of defects, leading to the formation of an amorphous layer. No obvious irradiation induced bubbles and amorphization is observed in the areas outside the end of range for the ions areas, marking the dose level at which amorphization occurs between 1-3 dpa and 3at%He, as shown in Fig. 4 (c).

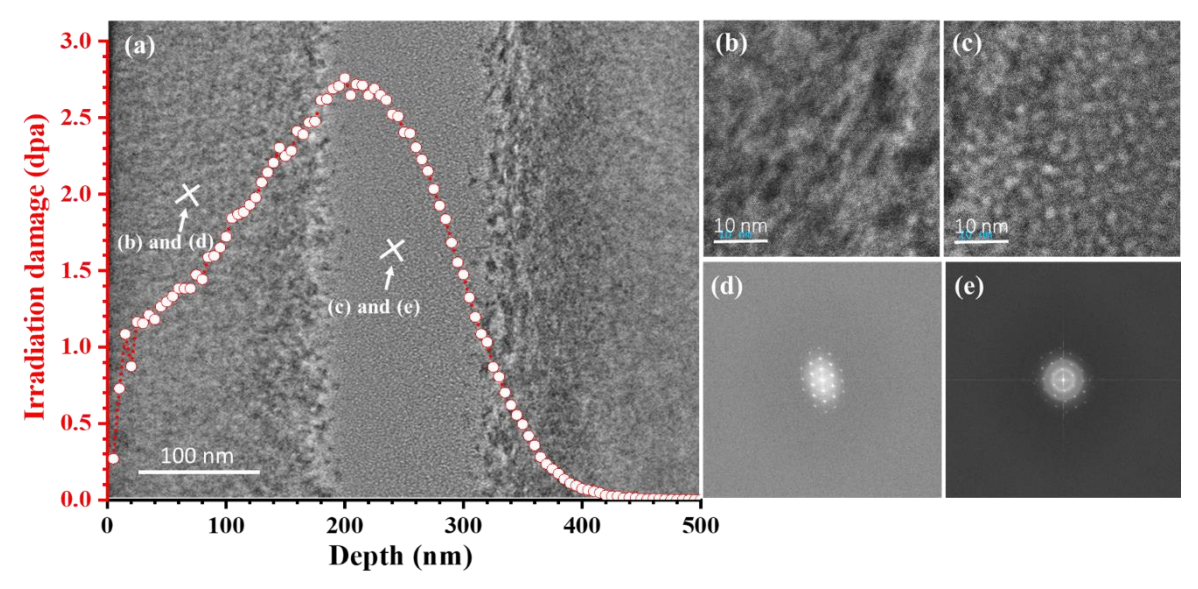


Figure 4 The cross-sectional TEM images and corresponding FFT patterns of Si implanted with He ions to a fluence of 1.0×10<sup>17</sup> ions/cm<sup>2</sup>: (a) the cross-sectional TEM images of implanted layer; (b) and (d) the enlarged image marked in image (a) and corresponding FFT pattern; (c) and (e) the enlarged images marked in image (a) and corresponding FFT pattern.

The cross-sectional TEM micrographs and SAED patterns of implanted sample with 7.5×10<sup>17</sup> ions/cm<sup>2</sup> He ions are shown in Fig. 5. Fig. 5 (a) shows a low magnification TEM image of the implantation region, in which an obviously amorphous layer is observed along perpendicular to the implantation direction. The swelling height of 78.0 nm is deduced from the cross section of the thin slice taken from interface between irradiated/unirradiated zone. According to the enlarged TEM images Figs. 5 (b) and (c) and SAED patterns, it can be found that three distinct zones are clear for this fluence: amorphous layer with the bubble size of 1-2 nm in diameters, defect layer, and matrix. It is well known that multiple aspects including radiation induced phase transformation, generated defects, and implanted ions are contributed to the swelling of Si with He implantation <sup>28</sup>. The amorphous layer decreases the density of Si and therefore contributes to swelling 41,42. Furthermore, the formation of bubbles in the also contributes to the swelling height of Si. The estimated swelling height contribution from the amorphous phase transformation is estimated to be 7 nm based on the density change of amorphous Si 32. Therefore, it can be inferred that the contribution of the swelling height from the bubbles should be 71 nm. To summarize the above statements, the current results show that the swelling is mainly attributed to the bubbles formation.

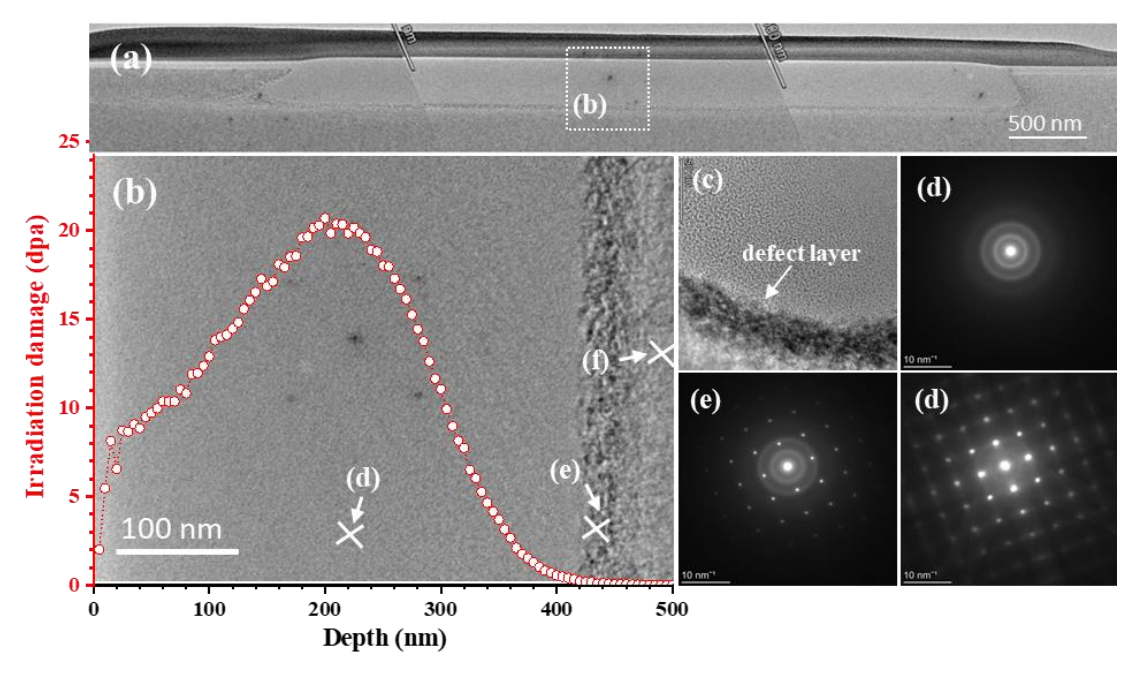
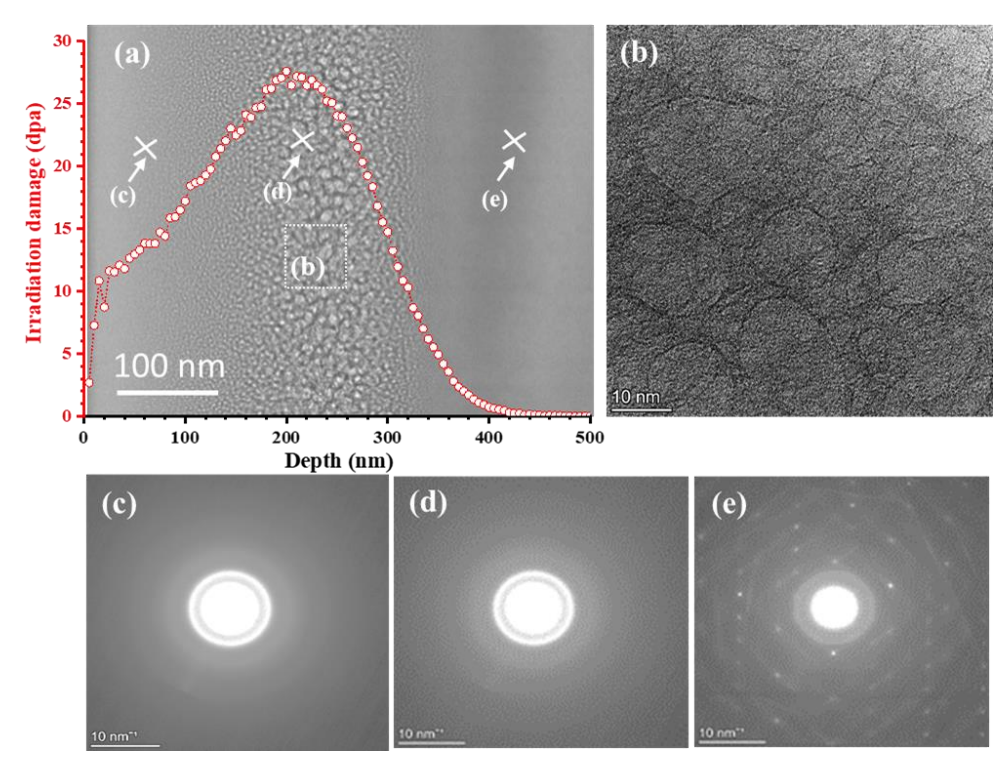


Figure 5 The cross-sectional TEM images and corresponding SAED patterns of Si implanted with He ions to a fluence of 7.5×10<sup>17</sup> ions/cm<sup>2</sup>: (a) low magnification TEM image of the implanted area; (b) the enlarged image of position (b) marked in image (a); (c) the enlarged image of position (c) marked in image (b); (d) to (f) the SAED patterns located at different positions marked in image (b).

The cross-section micrographs and corresponding SAED patterns of Si (001) implanted with the highest fluence ( $1.0 \times 10^{18}$  ions/cm<sup>2</sup>) are exhibited in <u>Fig. 6</u>. The TEM images display that He implantation induced the formation of bubbles, and the density and size of these bubbles vary with depth. The total damage layer in Si (100) is measured to be 447 nm from the TEM images, as shown in <u>Fig. 6 (d)</u>, while it is about 420 nm from the results of SRIM. <u>The apparent discrepancy is attributed to the increment in the porosity of Si with the enhanced He concentration.</u> SAED patterns also illustrate the depth position at which a transition from crystalline to amorphous in Si (100) is occurred, as shown in <u>Fig. 6 (a) to (c)</u>. Comparing fluences, implantation with a fluence of  $1.0 \times 10^{17}$  ions/cm<sup>2</sup> produces partial amorphization, while an implantation fluence of  $1.0 \times 10^{18}$  ions/cm<sup>2</sup> exhibits total amorphization. In addition, the thickness of amorphous layer increases with implantation fluences, as shown in <u>Fig. 5</u> and <u>6</u>.



<u>Figure 6</u> The cross-section micrographs and corresponding SAED patterns of Si (001) implanted with 1.0×10<sup>18</sup> ions/cm<sup>2</sup>: (a) low magnification TEM image of the implanted area; (b) the enlarged image of position (b) marked in image (a); (c)-(e) the SAED patterns at different positions.

Fig. 7 exhibits the experimental results of the <u>bubble diameter distribution</u>, bubble density, and cumulative swelling height as a function of implantation depth for the fluence of 1.0×10<sup>18</sup> ions/cm<sup>2</sup>. The bubbles formation extends to the implanted surface from one side and to the maximum implantation depth approaching uniform and small, while becoming non-uniform and larger at the implantation depth from 201.0 nm to 382.0 nm. According to Fig. 7 (a) to (c), the smallest average bubble diameter is 2.3±0.6 nm approaching the surface, and the largest bubble diameter reaches up to 17.2±9.89 nm at the depth of 320.0 nm. The average values reported here are based on 20 TEM images. Furthermore, the bubble density profile follows a similar trend to the average diameter of bubbles distribution. In addition, the void swelling in Si follows nearly a Gaussian distribution, with a maximum volumetric swelling around 0.022 at the depth of 320 nm. The method employed to calculate the volumetric swelling of Si is adopt from the reference<sup>43</sup>. S. Leclerc et al. investigated the swelling behavior of SiC under helium implantation and proposed that amorphization and helium bubbles are the main reasons to cause the swelling <sup>28</sup>. Furthermore, Y. Yang et al. proposed that the swelling height caused

by the helium bubbles can be calculated by using fractal volumetric swelling <sup>44</sup>. The cumulative swelling height of Si calculated from Y. Yang's model as a function of implantation depth is also illustrated in Fig. 7. The calculated swelling height for samples implanted with the fluence of 1.0×10<sup>18</sup> ions/cm<sup>2</sup> is about 105.4 nm based on the Yang's model <sup>44</sup>, which is a slightly higher than the height measured by AFM (97 nm), as shown in Fig. 2. The reason for the different swelling height measured by TEM and AFM is attributed to the heterogeneous distribution of bubbles in Si along the implantation depth, as shown in Fig. 7. It is noted that the size distribution of the bubbles is a bimodal distribution at the high fluence region, especially at the peak values of He concentration/dpa, as shown in Fig. 7 (c). For simplicity, we utilize the average bubble diameter to calculate the accumulative swelling in the current investigation, realizing that this might lead to a small overestimation of swelling height.

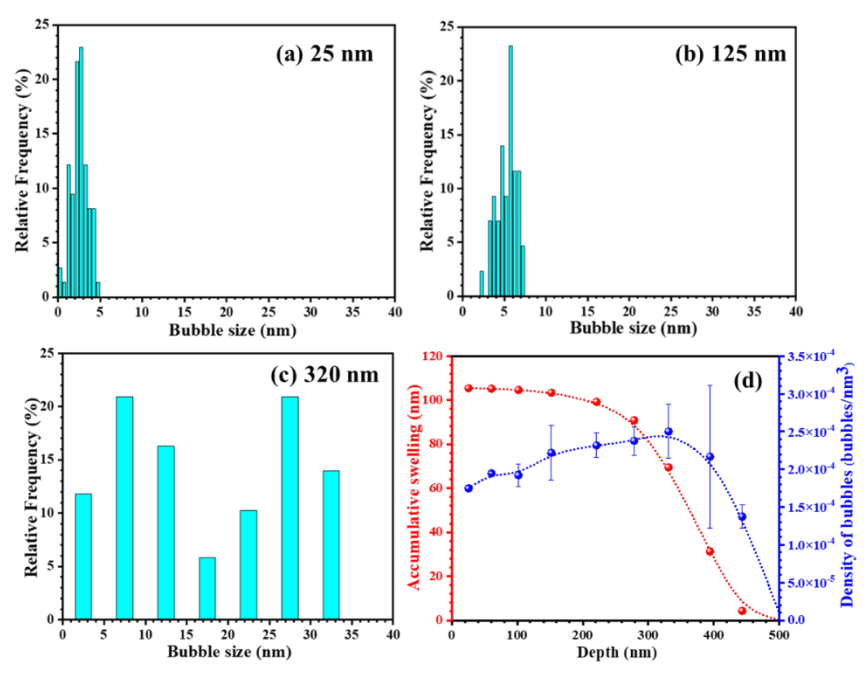
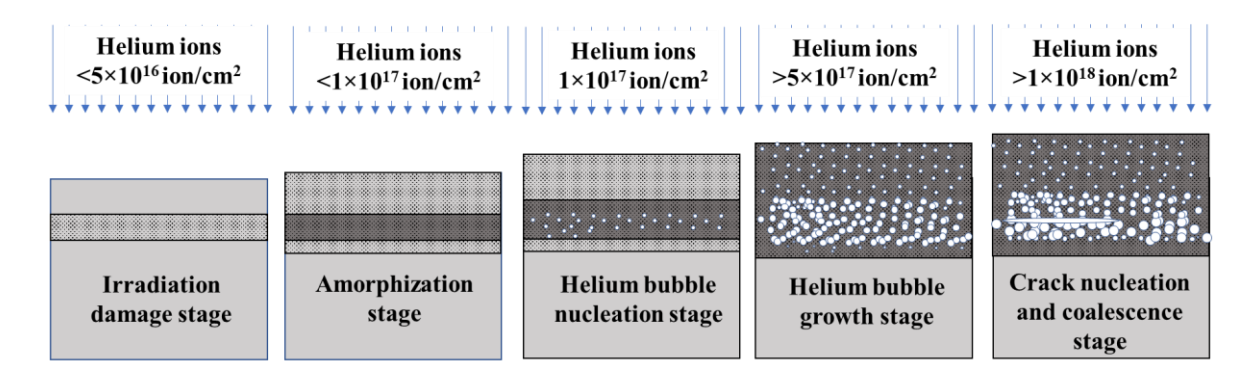


Figure 7 Bubble size distribution, bubble density, and cumulative swelling height resolved in depth for the fluence of 1×10<sup>18</sup> ions/cm<sup>2</sup>: (a)-(c) bubble size distribution at different depths; (d) bubble density and cumulative swelling height.

Based on the above results and statements, it can be found that in current experiments, the microstructure of Si under He implantation is determined by the fluences. Therefore, damage process can be divided into different states based on the alternation of microstructure and fluences, including irradiation damage stage, amorphization stage, He bubble nucleation stage,

He bubble growth stage, and stage of crack nucleation and coalescence. The structural changes as well as swelling as a function of fluences are schematically displayed in Fig. 8. At irradiation damage state, in which the implantation fluence is less than  $5.0 \times 10^{16}$  ions/cm<sup>2</sup>, irradiation induces the generation of defects, including interstitial clusters and vacancies, instead of the formation of bubbles and amorphization, as shown in Fig. 3. With the increasing of fluences from  $5.0 \times 10^{16}$  to less than  $1.0 \times 10^{17}$  ions/cm<sup>2</sup>, the damage process gets into the amorphization stage, in which irradiation induced the formation of amorphous layer in Si, as shown in Fig. 4. Since the binding energy between atoms is reduced by amorphization, the bubbles are easier to nucleate in the amorphous region. With the further rising of implantation fluences, more than  $7.5 \times 10^{17}$  ions/cm<sup>2</sup>, the entire implanted region gradually becomes amorphous. Meanwhile, the size of bubble gradually increases with the increasing of fluences. However, the heterogeneous distribution of bubbles in size and density along the implantation depth is formed because of the stopping of the Helium ions at the end of the range, as shown in Fig. 5. The size of voids gradually increases with the further increase of fluences. The voids will merge together and then a crack will be formed when the fluence increases to more than  $1.0 \times 10^{18}$  ions/cm<sup>2</sup> <sup>45</sup>.



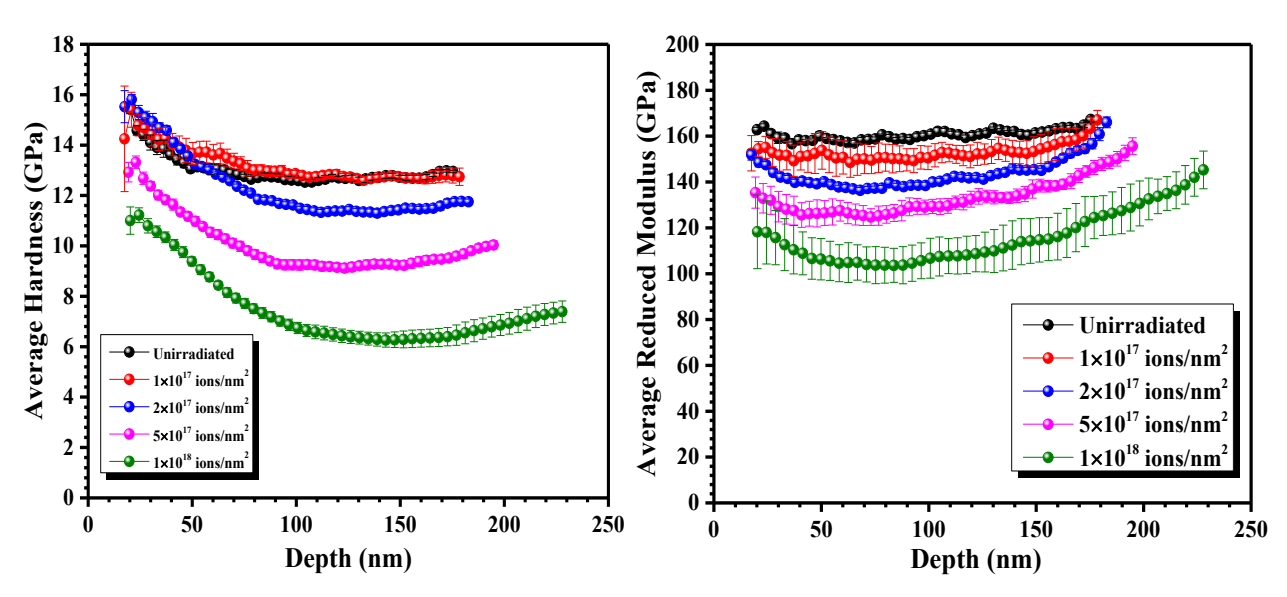
<u>Figure 8 Schematic cartoon of the structure and swelling evolution of Helium implanted Si as</u> a function of fluences.

Average hardness and reduced modulus variation with depth of samples with and without implantation are illustrated in <u>Fig. 9</u>. The results illustrate, as expected, that average reduced modulus gradually decreases as the implantation fluence rises. Average reduced modulus for fluences of  $1.0\times10^{18}$ ,  $5.0\times10^{17}$ ,  $2.0\times10^{17}$  and  $1.0\times10^{17}$  ions/cm<sup>2</sup> are about  $106.7\pm8.7$ ,  $129.4\pm10^{17}$ 

3.1,  $140.0 \pm 1.8$  and  $150.5 \pm 5.1$  GPa reported at depth of around 100 nm, respectively, which are smaller than that of unirradiated sample with 160.9±1.2 GPa. This result is widely consistent with results on self-ion implanted Si by D.M. Follstaedt et al., who reported a reduced hardness and elastic modulus after implantation <sup>46</sup>. The Si is completely amorphous after 50 dpa of implantation and thus the elastic modulus is between 130-140 GPa depending on the substrate orientation. This result is slightly higher than our current samples implanted with 5.0×10<sup>17</sup> ions/cm<sup>2</sup>, which the peak dose is around 50 dpa, because no bubbles are formed after self-ions implantation. In addition, the average reduced modulus gradually increases with the increasing of penetration depth, which may be caused by the effect of the substrate beneath the implantation layer. It is generally accepted that the elastic modulus of materials will not change significantly with the alteration of the indentation depth as it is assumed to be a structure-insensitive property <sup>47</sup>. However, for implanted samples, the reduced modulus first declines with depth and then rises and approaches bulk values at deep penetration. The explanation for this phenomenon is the fact that both amorphization of the Si and development of He bubbles reduce the overall elastic modulus <sup>48</sup>. In addition other work assumed that the plastic deformation zone beneath the indentation can be approximated as a hemisphere with a radius of 5-10 times the penetration depth <sup>49,50</sup>. Using this assumption in the current experiments, the plastic zone gradually expands into the unirradiated Si substrate with increasing of the penetration depth, resulting in a gradual increase of the elastic modulus back to bulk property of 161 GPa at deep indentation depths.

With regards to the average hardness, however, it first increases before declining with increase implantation fluences at the depths bellow 75 nm. Average hardness for fluences of  $1.0\times10^{18}$ ,  $5.0\times10^{17}$ ,  $2.0\times10^{17}$ ,  $1.0\times10^{17}$  ions/cm<sup>2</sup> and unimplanted sample are  $9.4\pm0.2$ ,  $11.0\pm0.2$ ,  $13.3\pm0.1$ ,  $13.7\pm0.4$  and  $13.1\pm0.2$  GPa, respectively. when penetration depth extends to more than 75 nm, there is no obvious difference between unimplanted and implanted samples with  $1.0\times10^{17}$  ions/cm<sup>2</sup> in terms of the average hardness measurement. However, the average hardness gradually declines with the further rising of implantation fluences due to the microstructure changes of Si. In addition, a decrease in hardness with increasing indent depth

is observed. Such depth dependent hardness behavior is attributed to the indentation size effect (ISE) phenomena <sup>51</sup>. The AFM surface topographic image of implanted areas with different implantation fluence after nanoindentation testing is shown in Figs. 10 (a) and (b). In addition, the relationship between pile up height and implantation fluence is also illustrated in Fig. 10 (c). The results indicate that no significant change in pile-up or sink-in behavior as a function of fluence is observed. It is well known that the irradiation induced hardening behavior of materials is primary attributed to the irradiation induced defects <sup>52</sup>. For Si implanted with a low fluence, for example 1.0×10<sup>17</sup> ions/cm<sup>2</sup>, the diameter of bubbles is small, and the implantation layer is not completely transformed from a crystalline to amorphous state. Therefore, irradiation induced hardening behavior mainly can be associated to the bubbles and defect clusters rather than irradiation induced amorphization. As the size of bubbles gradually increases with the rising of implantation fluence, the irradiation induced defects effect gradually diminishes since they get absorbed by the bubble boundaries <sup>53</sup>. But even the large He bubbles still contribute to the hardness increase of Si based on the Orowan model <sup>54</sup>. However, when implantation fluence increases to 2.0×10<sup>17</sup> ions/cm<sup>2</sup>, as shown in Fig. 9, the hardness reduced significantly. A similar behavior reported by C.L. Xu et al., who investigated the hardening behavior of 6H-SiC under Ne8+ ion irradiation, and they attributed this phenomenon to the dose threshold of lattice amorphization in SiC irradiated at RT 55. With the further increasing of implantation fluence, a softening behavior in hardness is observed because a amorphized layer is formed and the size of bubbles approaches a critical value <sup>55,56</sup>.



<u>Figure 9</u> Average hardness (left) and average reduced modulus (right) variation with depth for different implantation fluences.

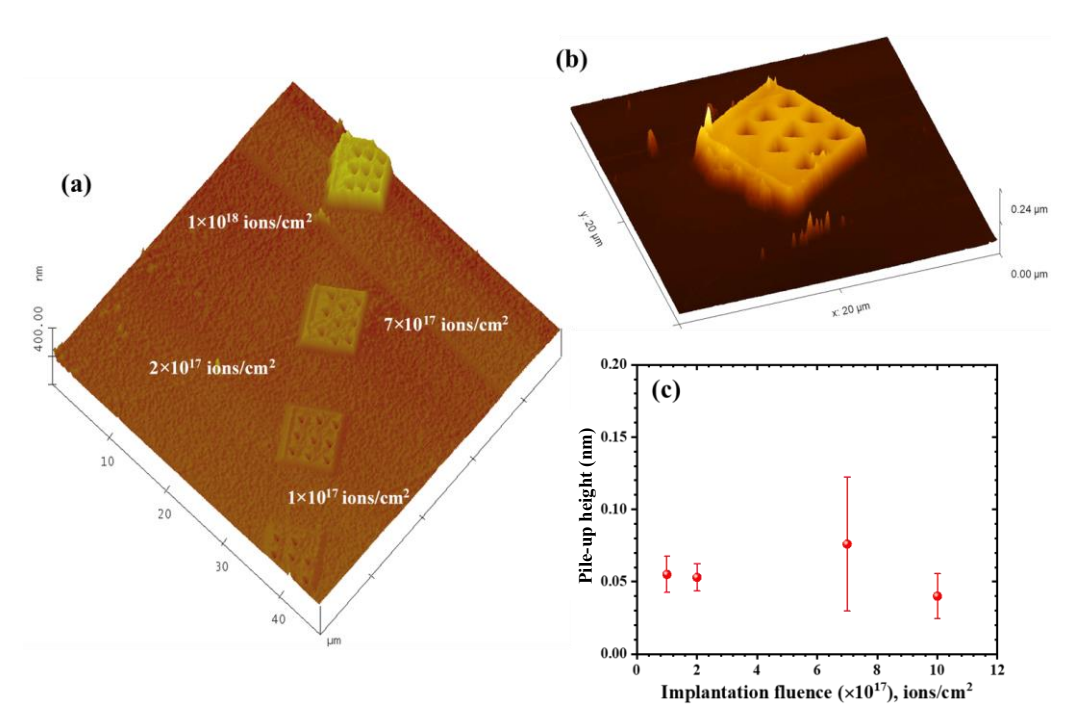


Figure 10 The AFM surface topographic image of implanted areas and corresponding pile-up height:

(a) AFM image of irradiated area; (b) the enlarged AFM image of area implanted with 1×10<sup>18</sup>

ions/cm<sup>2</sup>; (c) the relationship between pile-up height and implantation fluence.

# 4. Conclusions

In the present work, the relationship among the swelling behavior, microstructure, and micromechanical properties of Si (100) under 25 keV He implantation with different fluences at RT were investigated. The conclusions are as follows:

- (1) The swelling height gradually increases with the rising of implantation fluence, and their relationship follows a linear law. No blistering is observed even as implanted fluence is extended to  $1.0 \times 10^{18}$  ions/cm<sup>2</sup>.
- (2) Interstitial clusters rather than He bubbles are visible in bright-filed TEM images of Si implanted with fluences of  $5.0\times10^{16}$  ions/cm<sup>2</sup>. A mixed layer consisting of amorphous and matrix with small size bubbles is observed at a fluence of  $1.0\times10^{17}$  ions/cm<sup>2</sup>. As the fluence reaches  $1\times10^{18}$  ions/cm<sup>2</sup>, a completely amorphous layer with a larger number of bubbles is observed. The density and average diameter of bubbles close to the implanted surface and to the maximum implantation depth are uniform and small, while bubbles are non-uniform and large in the middle of the implantation layer. The swelling and property change due to helium implantation are a mixture between amorphization, helium bubble formation, and vacancy concentration.
- (3) The average reduced modulus gradually declines with implantation fluence due to the reduction of density of the implantation layer, while the average hardness goes through a maximum.

## Acknowledgements

This publication was made possible in part by NSF/DMRMRI1338139. The research was performed using funding received from the National Science Foundation's division of materials research, USA under the award number 1807822. The samples were FIB-milled and Heimplanted at the Biomolecular Nanotechnology Center/QB3 at UC Berkeley. The TEM was performed at The Molecular Foundry, which is supported by the Office of Science, Office of Basic Energy Sciences, of the U.S. Department of Energy under Contract No. DE-AC02-05CH11231

#### **Author Declarations**

#### **Conflict of Interest**

The authors have no conflicts to disclose.

## **Ethics Approval**

Ethics approval is not required.

## **Data Availability**

The data that support the findings of this study are available within the article and from the corresponding authors upon reasonable request.

#### References

- <sup>1</sup> G.S. Was, Z. Jiao, E. Getto, K. Sun, A.M. Monterrosa, S.A. Maloy, O. Anderoglu, B.H. Sencer, and M. Hackett, Scripta Materialia **88**, 33 (2014).
- <sup>2</sup> B. Heidrich, S.M. Pimblott, G.S. Was, and S. Zinkle, Nuclear Instruments and Methods in Physics Research Section B: Beam Interactions with Materials and Atoms **441**, 41 (2019).
- <sup>3</sup> J.S. Williams, Materials Science and Engineering: A **253**, 8 (1998).
- <sup>4</sup> S.J. Pearton, Materials Science Reports 4, 313 (1990).
- <sup>5</sup> M. Maldovan, Nature Mater **14**, 667 (2015).
- <sup>6</sup> J. Maire, R. Anufriev, R. Yanagisawa, A. Ramiere, S. Volz, and M. Nomura, Sci. Adv. **3**, e1700027 (2017).
- <sup>7</sup> M. Nomura, J. Shiomi, T. Shiga, and R. Anufriev, Jpn. J. Appl. Phys. **57**, 080101 (2018).
- <sup>8</sup> W. Wesch, Nuclear Instruments and Methods in Physics Research Section B: Beam Interactions with Materials and Atoms **68**, 342 (1992).
- <sup>9</sup> W. Wesch, E. Wendler, and C.S. Schnohr, Nuclear Instruments and Methods in Physics Research Section B: Beam Interactions with Materials and Atoms **277**, 58 (2012).
- <sup>10</sup> C.C. Griffioen, J.H. Evans, P.C. De Jong, and A. Van Veen, Nuclear Inst. and Methods in Physics Research, B **27**, 417 (1987).
- <sup>11</sup> B.S. Li, Y.Y. Du, Z.G. Wang, T.L. Shen, Y.F. Li, C.F. Yao, J.R. Sun, M.H. Cui, K.F. Wei, H.P. Zhang, Y.B. Shen, Y.B. Zhu, and L.L. Pang, Nuclear Instruments and Methods in Physics Research, Section B: Beam Interactions with Materials and Atoms **337**, 21 (2014).
- <sup>12</sup> P.F.P. Fichtner, J.R. Kaschny, R.A. Yankov, A. Mücklich, U. Kreißig, and W. Skorupa, Applied Physics Letters **70**, 732 (1997).
- <sup>13</sup> E. Oliviero, M.F. Beaufort, and J.F. Barbot, Journal of Applied Physics **90**, 1718 (2001).
- <sup>14</sup> D.L. da Silva, P.F.P. Fichtner, M. Behar, A. Peeva, R. Koegler, and W. Skorupa, Nuclear Instruments and Methods in Physics Research Section B: Beam Interactions with Materials and Atoms **190**, 756 (2002).
- <sup>15</sup> W.T. Han, H.P. Liu, and B.S. Li, Applied Surface Science **455**, 433 (2018).
- <sup>16</sup> J.H. Evans, Nuclear Instruments and Methods in Physics Research Section B: Beam Interactions with Materials and Atoms **196**, 125 (2002).
- <sup>17</sup> X. Cheng, Z. Feng, C. Li, C. Dong, and X. Li, Electrochimica Acta **56**, 5860 (2011).

- <sup>18</sup> M. Ikeyama, K. Saitoh, S. Nakao, H. Niwa, S. Tanemura, Y. Miyagawa, and S. Miyagawa, in 1998 International Conference on Ion Implantation Technology. Proceedings (Cat. No.98EX144) (IEEE, 1999), pp. 736–739.
- <sup>19</sup> P.K. Giri, V. Raineri, G. Franzo, and E. Rimini, Physical Review B 65, 012110 (2001).
- <sup>20</sup> S. Momota, J. Zhang, T. Toyonaga, H. Terauchi, K. Maeda, J. Taniguchi, T. Hirao, M. Furuta, and T. Kawaharamura, Journal of Nanoscience and Nanotechnology **12**, 552 (2012).
- <sup>21</sup> J. Zhang, S. Momota, T. Toyonaga, H. Terauchi, F. Imanishi, and J. Taniguchi, Nuclear Instruments and Methods in Physics Research Section B: Beam Interactions with Materials and Atoms **282**, 17 (2012).
- <sup>22</sup> T. Wirtz, P. Philipp, J.-N. Audinot, D. Dowsett, and S. Eswara, Nanotechnology **26**, 434001 (2015).
- <sup>23</sup> S. Agarwal, Y. Lin, C. Li, R.E. Stoller, and S.J. Zinkle, Nuclear Instruments and Methods in Physics Research Section B: Beam Interactions with Materials and Atoms **503**, 11 (2021).
- <sup>24</sup> J. Chang, J. Cho, C. Gil, and W.-J. Lee, Nuclear Engineering and Technology **46**, 475 (2014).
- <sup>25</sup> P. Reinke, G. Francz, P. Oelhafen, and J. Ullmann, Phys. Rev. B **54**, 7067 (1996).
- <sup>26</sup> J.D. Arregui-Mena, T. Koyanagi, E. Cakmak, C.M. Petrie, W.-J. Kim, D. Kim, C.P. Deck, C. Sauder, J. Braun, and Y. Katoh, Composites Part B: Engineering **238**, 109896 (2022).
- <sup>27</sup> K.M. Tynyshbayeva, K.K. Kadyrzhanov, A.L. Kozlovskiy, Y.I. Kuldeyev, V. Uglov, and M.V. Zdorovets, Crystals **12**, 239 (2022).
- <sup>28</sup> S. Leclerc, A. Declémy, M.F. Beaufort, C. Tromas, and J.F. Barbot, Journal of Applied Physics **98**, 113506 (2005).
- <sup>29</sup> S. Eichler, J. Gebauer, F. Börner, A. Polity, R. Krause-Rehberg, E. Wendler, B. Weber, W. Wesch, and H. Börner, Physical Review B **56**, 1393 (1997).
- <sup>30</sup> R. Nipoti, G. Lulli, S. Milita, M. Servidori, C. Cellini, and A. Carnera, Nuclear Instruments and Methods in Physics Research Section B: Beam Interactions with Materials and Atoms **112**, 148 (1996).
- <sup>31</sup> K.J. Abrams, J.A. Hinks, C.J. Pawley, G. Greaves, J.A. van den Berg, D. Eyidi, M.B. Ward, and S.E. Donnelly, Journal of Applied Physics **111**, 083527 (2012).
- <sup>32</sup> J.S. Custer, M.O. Thompson, D.C. Jacobson, J.M. Poate, S. Roorda, W.C. Sinke, and F. Spaepen, Appl. Phys. Lett. **64**, 437 (1994).
- <sup>33</sup> F.I. Allen, P. Hosemann, and M. Balooch, Scripta Materialia **178**, 256 (2020).
- <sup>34</sup> V. Raineri, S. Coffa, E. Szilágyi, J. Gyulai, and E. Rimini, Phys. Rev. B **61**, 937 (2000).
- <sup>35</sup> R. Siegele, G.C. Weatherly, H.K. Haugen, D.J. Lockwood, and L.M. Howe, Appl. Phys. Lett. **66**, 1319 (1995).
- <sup>36</sup> V.F. Reutov and A.S. Sokhatskii, Tech. Phys. Lett. **28**, 615 (2002).
- <sup>37</sup> M.L. David, M.F. Beaufort, and J.F. Barbot, Nuclear Instruments and Methods in Physics Research Section B: Beam Interactions with Materials and Atoms **226**, 531 (2004).
- <sup>38</sup> K. E. Haynes, "Defect Evolution during Elevated-Temperature Helium Ion Implantation into Silicon," Ph.D. thesis (University of Florida, 2019).
- <sup>39</sup> F.F. Morehead and B.L. Crowder, Radiation Effects **6**, 27 (1970).
- <sup>40</sup> V.F. Reutov and A.S. Sokhatskii, Technical Physics Letters **28**, 615 (2002).

- <sup>41</sup> V. Heera, F. Prokert, N. Schell, H. Seifarth, W. Fukarek, M. Voelskow, and W. Skorupa, Applied Physics Letters **70**, 3531 (1997).
- <sup>42</sup> O.W. Holland, J.D. Budai, and C.W. White, Applied Physics Letters **57**, 243 (1990).
- <sup>43</sup> M. Terasawa, M. Shimada, and S. Nakahigashi, Journal of Nuclear Science and Technology **19**, 646 (1982).
- <sup>44</sup> Y. Yang, D. Frazer, M. Balooch, and P. Hosemann, Journal of Nuclear Materials **512**, 137 (2018).
- <sup>45</sup> X. Duo, W. Liu, S. Xing, M. Zhang, X. Fu, C. Lin, P. Hu, S.X. Wang, and L.M. Wang, J. Phys. D: Appl. Phys. **34**, 5 (2001).
- <sup>46</sup> D.M. Follstaedt, J.A. Knapp, and S.M. Myers, J. Mater. Res. **19**, 338 (2004).
- <sup>47</sup> P. Haušild, Journal of Nuclear Materials **551**, 152987 (2021).
- <sup>48</sup> Y. Yang, D. Frazer, M. Balooch, and P. Hosemann, Journal of Nuclear Materials **512**, 137 (2018).
- <sup>49</sup> M. Mata, O. Casals, and J. Alcalá, International Journal of Solids and Structures **43**, 5994 (2006).
- <sup>50</sup> A. Kareer, A. Prasitthipayong, D. Krumwiede, D.M. Collins, P. Hosemann, and S.G. Roberts, Journal of Nuclear Materials **498**, 274 (2018).
- <sup>51</sup> R. Kasada, Y. Takayama, K. Yabuuchi, and A. Kimura, Fusion Engineering and Design **86**, 2658 (2011).
- <sup>52</sup> R. Schaeublin, D. Gelles, and M. Victoria, Journal of Nuclear Materials **307–311**, 197 (2002).
- <sup>53</sup> O. El-Atwani, J.E. Nathaniel, A.C. Leff, B.R. Muntifering, J.K. Baldwin, K. Hattar, and M.L. Taheri, Journal of Nuclear Materials **484**, 236 (2017).
- <sup>54</sup> J. Gan and G.S. Was, Journal of Nuclear Materials **297**, 161 (2001).
- <sup>55</sup> C.L. Xu, C.H. Zhang, J.J. Li, L.Q. Zhang, Y.T. Yang, Y. Song, X.J. Jia, J.Y. Li, and K.Q. Chen, in Nuclear Instruments and Methods in Physics Research, Section B: Beam Interactions with Materials and Atoms (2012).
- <sup>56</sup> J. Li, H. Huang, G. Lei, Q. Huang, R. Liu, D. Li, and L. Yan, Journal of Nuclear Materials **454**, 173 (2014).